Multipurpose Acoustic Metamaterial Anchors for Aluminum Scandium Nitride Contour Mode Resonators

Xuanyi Zhao[®], Onurcan Kaya[®], Tommaso Maggioli, and Cristian Cassella[®], Member, IEEE

Abstract—We present a new design for AlScN contour-moderesonators (CMRs) operating in the radiofrequency (RF) range. This design relies on acoustic metamaterials (AM) based lateral anchors to greatly enhance the power handling compared to conventional CMR-designs. Such anchors generate acoustic stopbands that prevent the leakage of piezo-generated acoustic energy from the resonating body into the substrate. The AM anchors reported in this work consist of the same AlScN film as in the CMRs' active region, combined with a periodic array of SiO2 rods. Their use allows a reduction of CMRs' thermal resistance with respect to conventional designs, and enables a significant temperature compensation. As a result, the CMRs with AM anchors reported in this work show a ~60% reduction in their Duffing coefficient with respect to conventional designs with fully-etched lateral sides, hence an improved linearity. Furthermore, when used to set the output frequency of high-power feedback loop oscillators, the CMRs with the AM anchors reported here enable a lower phase-noise compared to what achievable when employing the conventional counterparts.

Index Terms— Aluminum scandium nitride, microacoustic resonators, acoustic metamaterials, contour mode resonators, phase noise.

I. Introduction

N THE last decades, Aluminum Nitride (AlN) microacoustic resonators [1], [2], [3], [4], [5], [6], [7] have been critical components of radiofrequency (RF) front-ends in cellular handsets. When assembled in networks, the use of these devices has enabled the proliferation of low-loss filters covering a large number of service bands [8], [9], [10]. With the advent of the fifth-generation (5G) communication standard, AlN has soon became inadequate to cover the more stringent bandwidth needs. As a result, RF microacoustic resonators using Aluminum Scandium Nitride (AlScN) as a piezoelectric layer are becoming more and more popular.

When substituting AlN with AlScN, the achievable piezoelectric coupling coefficient for any targeted mode of vibration is enhanced, leading to a boosted electromechanical coupling coefficient (k_t^2) [11], [12], [13], [14], [15], [16], [17], [18].

Manuscript received 6 March 2024; revised 18 April 2024; accepted 3 May 2024. Date of publication 16 May 2024; date of current version 2 August 2024. This work was supported by the National Science Foundation (NSF) through the CAREER Award under Grant 2034948. Subject Editor E. S. Kim. (Corresponding author: Xuanyi Zhao.)

The authors are with the Department of Electrical and Computer Engineering, Northeastern University, Boston, MA 02115 USA (e-mail: zhao.xuan@northeastern.edu).

Color versions of one or more figures in this article are available at https://doi.org/10.1109/JMEMS.2024.3399593.

Digital Object Identifier 10.1109/JMEMS.2024.3399593

Since the bandwidth of any microacoustic filter is proportional to the k_t^2 value of its resonators, the use of AlScN enables RF filters with wider bandwidths than AlN. Nonetheless, such replacement comes with additional design challenges. One of the most critical challenges is the lower thermal conductivity that AlScN exhibits compared to AlN [19], [20], [21]. Due to the reduction in thermal conductivity, and since the nonlinearities of AlN and AlScN piezoelectric resonators arise from thermal effects (i.e., from heat generated into the active region during the motion [22], [23], [24], [25], [26]), using anchoring schemes validated for AlN resonators in AlScN counterparts leads to worse linearity. At the same time, when assuming the typical anchoring strategy, increasing the anchors' width to favor the heat flow into the substrate results into quality factor degradations due to anchor losses [24], [27], [28], [29], [30]. These degradations become even more significant when targeting higher frequencies of operation and impedance matching to 50 Ω .

AlN piezoelectric resonators have been also used as frequency references in oscillators for timing applications and as resonant sensors in closed-loop read-out schemes [31], [32], [33]. For both application scenarios, a transition from AlN to AlScN enables a lower power consumption for the controlling electronic circuit. However, when used for timing applications, the lower power handling capabilities of AlScN devices results into increased phase-noise levels in oscillators compared to what achievable with AlN devices (even when assuming the same quality factor). In fact, when the resonator used as frequency reference in an oscillator operates nonlinearly, a larger amplitude-to-phase noise (AM-to-PM) conversion is generated in the oscillator's phase noise [34]. Similarly, nonlinearities in resonant sensors lead to lower dynamic ranges in closed-loop read-out schemes, heavily degrading the minimum achievable limit-of-detection [35].

In order to overcome these challenges and reduce the gap in linearity between AlN and AlScN resonators, our group has recently developed a new approach to anchor AlScN devices along their lateral direction [30]. This approach is centered around the adoption of acoustic metamaterial (AM) anchors. Differently from conventional anchors, AM anchors exhibit regions of inhibited propagation that can be used to prevent energy leakage into the Si-substrate along the main vibrational direction. At the same time, AM anchors enable a higher heat flow from the resonators' active region into the substrate. As a result, using AM anchors reduces the resonators'

1057-7157 © 2024 IEEE. Personal use is permitted, but republication/redistribution requires IEEE permission. See https://www.ieee.org/publications/rights/index.html for more information.

thermal resistance (R_{th}) and their Duffing nonlinear coefficient (α_d [24], [36], [37]). A reduction of α_d leads to extended linearity in suspended AlN or AlScN devices [38].

In our previous work [30], we have demonstrated the effectiveness of AM anchors relying on a corrugated AlScN film. Unfortunately, these AM anchors are not manufacturable with enough reliability to be compatible with a mass-scale production. Also, the extent of the Rth reduction is inversely proportional to the thickness of the thinnest AlScN portion in the anchor. Therefore, the corrugation of the AlScN film intrinsically comes with a higher R_{th} than what we would be able to achieve if the AlScN film could preserve the same thickness used in the resonators' active region. Such discrepancy is even bigger when the AlScN film in AM anchors is processed to have a larger thickness variation across the AM anchors' length [30], [39]. Finally, while reducing R_{th} is key to extend the linearity of AlScN microacoustic resonators, α_d also depends on other factors, namely the mechanical figureof-merit (FoM) and the temperature-coefficient-of-frequency (TCF).

In this article, we surpass the limitations of our previously demonstrated AM anchors. We demonstrate AM anchors formed by the same uncorrugated AlScN film used in the active region of an AlScN contour-mode-resonator (CMR) [2], [4], together with a periodic array of thick SiO₂ rods. These rods extend along the in-plane direction (i.e., the y-direction) orthogonal to the CMR's main direction of motion (i.e., the x-direction). The AM anchors reported here provide a significant reduction of $R_{\rm th}$ by enabling the adoption of a larger anchoring perimeter with shorter anchor length. The adoption of the SiO₂ rods also allows an effective TCF reduction. Conjointly, the reduced R_{th} and decreased TCF lead to an extended linearity. We have verified that the improvement in linearity enabled by the adoption of the reported AM anchors enables better phase-noise in a high-power oscillator compared to what achievable when using conventional CMR designs with fully-etched lateral sides.

II. PRINCIPLE OF OPERATION

The AM anchors we have developed in this work can be described as finite chains of unit-cells deposited along the lateral sides of a CMR (Fig. 1). Each unit-cell consists of a SiO₂ rod deposited on top of a Pt-AlScN bilayer plate. The periodic nature of the AM anchors alters the dispersion of longitudinal modes displacing along the x-direction, creating regions of inhibited propagation (i.e., stopbands). Within these regions, the acoustic wave remains confined within the CMR's active region, allowing to preserve a high quality factor at its series resonance frequency (Q_s) despite the fact that the CMR's lateral sides are not fully-etched as in conventional designs. When comparing AM anchors with conventional metal Bragg reflectors (mBRs), an important distinction must be drawn: the bandgap that mBRs generate is significantly narrower than the bandgap generated by AM anchors [30]. As a result, differently from mBR-based anchors, AM anchors' reflection bandwidth is insensitive to process variations. This makes the same AM anchor-design usable by CMRs operating over a wide range of frequencies. Within any

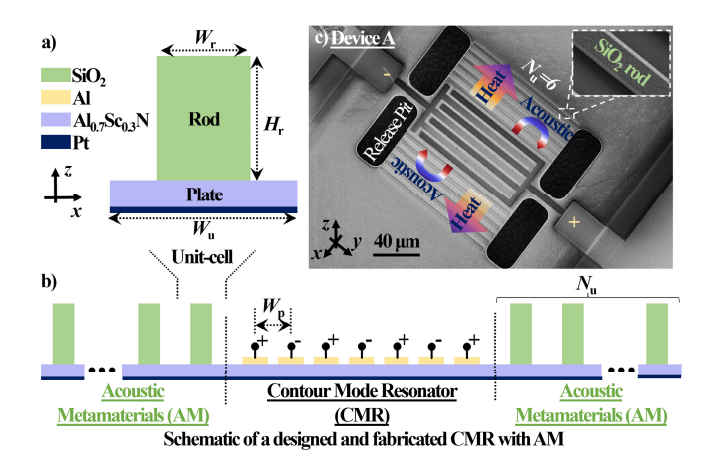


Fig. 1. Schematic view of (a) the AM anchors' unit-cell exploited in this work, and (b) their use to confine the lateral vibration of an AlScN contour-mode-resonator (CMR). (c) A Scanned Electron Microscope (SEM) picture of a fabricated CMR with the reported AM anchors is also shown. To note, the adopted AM design parameters in this primary design, labeled as "Device A", include: H_r =2.25 μ m, W_r =4 μ m, W_u =8 μ m, N_u =6, N_f =7.

stopband, the imaginary part of the AM anchors' wavevector (k_x) relative to longitudinal modes is proportional to the size of the stopband. This makes the attenuation per unit-meter that AM anchors generate when reached by longitudinal waves larger than what attainable when using mBRs. Hence, it allows to minimize the anchor losses along the CMR's lateral sides with a low number of unit-cells, $N_{\rm u}$ (i.e., through short lateral AM anchors connecting the CMR to the substrate). Being able to minimize the amount of anchor dissipations along the lateral side by engineering a short anchoring connection to the substrate allows to largely reduce $R_{\rm th}$ compared to conventional CMRs with etched lateral sides. The reduction of $R_{\rm th}$ is key to ease the heat-flow from the CMR's active region into the substrate and, consequently, to reduce the impact of thermal nonlinearities on the CMR's electrical response.

In our previous work [30], we demonstrated AM anchors using a corrugated AlScN film. This layer was formed by partially-etching the same AlScN layer used in a CMR's active region. This approach was effective in generating a confinement of the acoustic-wave within the CMR's active region, as well as in reducing R_{th} with respect to conventional CMR devices. However, generating a profiled AlScN layer requires a partial-etching step of the AlScN film, which is hard to perform reliably over entire silicon wafers. Also, the use of a grooved AlScN profile in the AM anchors comes with a higher R_{th} compared to what could be achieved if the same anchors could rely on the same AlScN thickness used in the CMR's active region.

We overcome this inefficiency by building AM anchors for AlScN CMRs not requiring any partial-etching of the AlScN layer. The AM anchors reported in this work are formed by an array of SiO₂ rods atop an un-etched AlScN layer. Using SiO₂ rods on the same AlScN layer used in the CMRs' active region makes it possible to achieve a certain degree of passive temperature compensation [40]. Through this compensation, the overall CMR's TCF reduces. The extent of this reduction depends on the ratio of the elastic energy stored in the AM

anchors' first unit-cells to the total elastic energy stored in the active region. This ratio is proportional to the CMR's number of fingers (i.e., to the mode number). Thanks to the reduction in TCF originated from the use of SiO_2 rods in the AM anchors, CMRs are affected even less by thermal nonlinearities (i.e., α_d is proportional to both R_{th} and TCF), thereby being able to handle more driving power.

III. DESIGN OF AM ANCHORS

A. Acoustic Dispersion Engineering

We used Finite Element Methods (FEM) to tackle the design of our AM anchors. We started by selecting a frequency of operation (420 MHz) for a targeted CMR. Then, we recurred to a dispersion analysis for one of the AM anchors' unit-cell by using Floquet periodicity. This analysis aimed to identify the unit-cell's dimensions producing a stopband around the CMR's targeted frequency of operation. During this step, we assumed the same thickness for the AlScN and Pt layers used in the CMR's active region. We report in Fig. 2-a the dispersion curves extracted around the targeted frequency of operation for our identified optimum unit-cell geometry. This optimum geometry includes a 2.25 μ m thick SiO_2 rod (i.e., $H_r = 2.25 \mu m$). After completing the design of the AM anchors' unit-cell, we verified their effectiveness in minimizing anchor losses along the CMR's lateral sides. This verification was performed by running a frequency-domain analysis wherein the CMR's interdigitated metal electrodes (IDTs) were driven by a voltage with frequency varying between 300 MHz and 500 MHz. Perfectly-Matched-Layers (PMLs) were incorporated in our simulations and positioned at the outer edges of the AM anchors. By looking at the achievable Q_s value vs. $N_u(\text{Fig. 2-b})$, we found that using six unit-cells is enough to minimize the anchor dissipations along the CMR's lateral sides. It is worth mentioning that the number of unit-cells required for the minimization of anchor losses is nearly half (6 vs. 11) of the one required when using the AM anchors adopted in [30]. In the following. we will label as "Device A" each CMR using seven fingers (N_f =7) in the active region and six copies of the optimized unit cell in each lateral AM anchor.

The design of the AM anchors' unit cell also requires identifying the width of each rod (W_r) . W_r can be expressed in terms of a design parameter, η , equal to the ratio of W_u to the width of the unit cell (W_r) . In Fig. 2-c, we compare the FEM-simulated admittance of Device A (using a η value equal to 0.5) with the admittances of two identical devices only differing in the adopted η value. The two devices consider the case of η equal to zero (i.e., no SiO₂ layer is used) and the case of η equal to 1 (i.e., a full SiO₂ layer plate is used). The modeshapes of their at-resonance total displacement can be found in Fig. 2-d. It is clear that anchor losses are unsustainable when no SiO₂ is used, leading to an over-damped electrical response. Using a not etched SiO₂ layer is also significantly worse than using SiO₂ rods.

B. Thermal Characterization

Nonlinearities in AlScN CMRs are mainly originated from thermal effects. When these resonators are driven by high

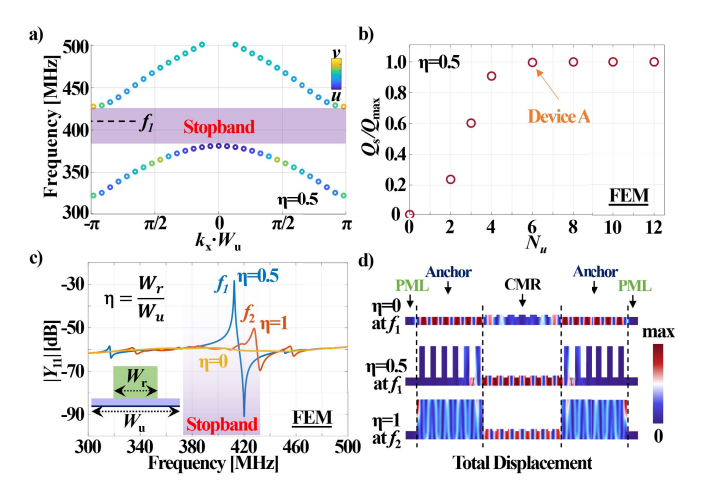


Fig. 2. a) FEM-simulated dispersion curves across for the AM unit-cell described in Fig. 1-a, within a frequency range close to the resonance frequency of the CMRs considered in this work (i.e., Device A); b) FEM-simulated trend of $Q_{\rm S}$ vs. $N_{\rm u}$, normalized to the maximum $Q_{\rm S}$ value achievable when assuming a quality factor value for all the remaining dissipation mechanisms of 1000. c) FEM simulated admittance of Device A (which uses a η value equal to 0.5, and of other two devices only differing in the adopted η value (zero or one). d) At-resonance modeshapes of the total displacement magnitude for the three CMRs described in (c).

power signals, the temperature increase produced during their motion generates a reduction of the AlScN Young's modulus that is proportional to the temperature reached. As a result, AlScN CMRs's resonance frequency lowers, a phenomenon often referred to as "softening" effect [38], [41], [42]. The dynamics governing the mechanical motion of CMRs for high driving power levels are well described by those of a mechanical resonator with a Duffing nonlinear term [24] that can be analytically estimated as:

$$\alpha_d = |TCF| \cdot R_{\text{th}} \cdot (R_{\text{m}} + R_{\text{s}}) \cdot (2\pi f_{\text{res}})^2 \tag{1}$$

As shown in Eq. (1), α_d is directly proportional to both $R_{\rm th}$ and TCF, while being inversely proportional to the CMR's figure-of-merit, FoM [i.e., (R_m+R_s) is inversely proportional to FoM, which is equal to $Q_s \cdot k_t^2$]. Therefore, when comparing the power-handling capabilities of different CMR designs with comparable FoM values, the design ensuring the highest power-handling can be identified by finding the one that has the lowest R_{th} ·TCF product. Hence, after identifying the minimum number of unit-cells (i.e. six unit-cells, see Fig. 2-b) in the AM anchors allowing to minimize the amount of anchor dissipations, we proceeded with the characterization of the AM anchors' thermal properties when the same number of unit-cells is considered. We started with R_{th} and with the CMR's thermal time constant (τ_{act}). While τ_{act} plays no role in CMRs' power-handling, its value determines the time required by CMRs' active-region to reach its steadystate temperature. τ_{act} also corresponds to the time required by CMRs to reach their steady-state resonance frequency value once power is injected through their IDTs. R_{th} and τ_{act} were extracted through FEM for both Device A and for a conventional CMR using the same active region's geometry but fully-etched lateral sides, which is labeled as "Device B" for the rest of the paper. The geometries and simulation set-up

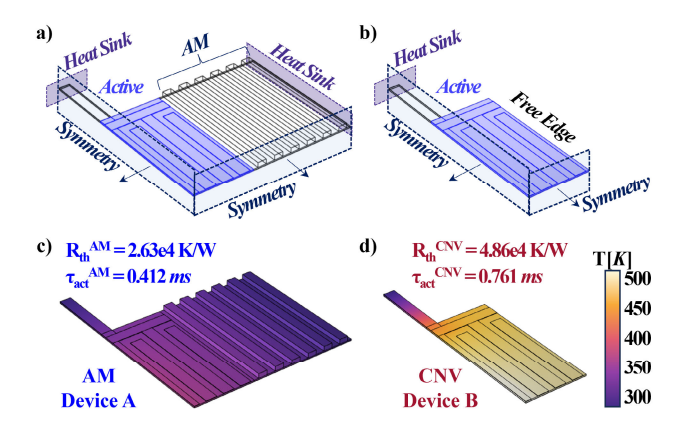


Fig. 3. a-b) Schematic view of the geometry we have used in our FEM simulations to analyze the thermal behavior of both (a) the CMR using the AM anchors reported in this work (Device A) and (b) a conventional CMR using fully-etched lateral sides (Device B). c-d) Simulated temperature distribution across the geometry used in our simulations for both the Device A and Device B.

we relied on during our thermal simulations are described in Fig. 3-a,b. In Fig. 3-c,d we report the temperature distribution for both investigated cases when assuming the substrate to be at ambient temperature and when a 1 mW power is injected in the center of the two CMRs' active region. Due to the high degree of symmetry in the investigated devices, our thermal simulations for both the conventional design and the design with AM anchors were run by considering only a quarter of the CMR's suspended region. Evidently, the adoption of the AM anchors allows Device A to achieve a nearly two times lower R_{th} value compared to the conventional device with fully-etched lateral sides (Fig. 3-c,d). This R_{th} -reduction comes with a comparable reduction in τ_{act} . In fact, despite the larger volume of the released area, the effective thermal capacitance (C_{th}) for Device A is comparable to the one of the conventional design. This is motivated by the fact that nearly no displacement is generated in the AM anchors. As a result, the only region really influencing the transient dynamics of the resonance frequency once the power is injected remains the Device A's active region.

After extracting R_{th} and τ_{act} for Device A, we studied its TCF through FEM. First, we investigated the dependence of TCF on the thickness of the SiO₂ rods (Fig. 4-a). As expected, we found that using taller rods enables a reduction in the magnitude of TCF. This reduction is motivated by the larger amount of elastic energy stored within the rods closest to the active region of the CMR. Consequently, the effect of a temperature increase on the modal stiffness of the CMR becomes less pronounced when the rods' thickness is higher. This is due to the increased amount of elastic energy stored in the SiO₂ rods. In fact, SiO₂ exhibits a TCE with opposite sign compared to AlScN, which is key to achieve a passive temperature compensation [40]. The degree of achievable temperature compensation is directly related to the ratio of the elastic energy stored in the SiO₂ rods to the one stored in the AlScN layer of the CMR's active region. This motivates why the overall TCF achieved by a CMR using AM anchors depends on the CMR's number of fingers (N_f) . In fact, the higher the number of fingers in the CMR's active region and

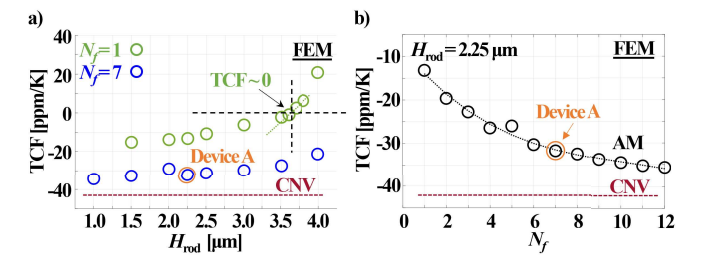


Fig. 4. Simulated TCF values using the same AM anchors as in Figure 2, but considering different thicknesses of the SiO_2 rods (H_r) and two different number of fingers in the CMR $[N_f]$ equal to 1 (in green) and 7 (in blue)]; b) Simulated TCF for N_u equal to 6, for the same H_r value we used in our experiment $(2.25\mu m)$ and for different numbers of fingers (N_f) in the CMR's active region.

the larger is the difference between the elastic energy stored in the CMR's active region and the one stored in the SiO₂ rods. In order to demonstrate this feature, we extracted TCF vs. the CMR's number of fingers (Fig. 2) when considering the optimal AM anchors' design and the same finger's design for the active region used by Device A. As expected we found that a higher number of fingers leads to higher TCF values approaching the TCF value achieved by a CMR with fully-etched lateral sides (Fig. 4-b). Given that CMRs with low numbers of fingers are more easily compensated by the SiO₂ rods in the AM anchors, it is useful to investigate the minimum SiO₂ thickness required to achieve a TCF equal to zero when relying on CMRs with only one finger (i.e., CMRs exploiting a fundamental lateral mode of vibration). We report in Fig. 4-a the trend of TCF vs. the SiO₂ thickness for a CMR with only one finger. We found that a 3.6 μ m-thick SiO₂ layer is needed for a full temperature compensation of a CMR with $N_{\rm f}$ equal to 1.

IV. FABRICATION

In order to experimentally characterize the performance of the AM anchors presented in this work, we built CMRs using optimized AM anchors along their side. The main steps of the fabrication process we relied on are described in Fig. 5. We started from a multi-layer stack deposition on a high resistivity silicon wafer. We first deposited a 20 nm-thick AlN seed layer by using reactive sputtering. Then, we sputtered a 80 nmthick Pt layer and co-sputtered a 500 nm AlScN film with a 30% scandium-doping concentration. The deposition of these three layers was run in the same chamber without breaking the vacuum. Then, we formed the release windows using inductively coupled plasma reactive-ion etching (ICP-RIE), as shown in Fig. 5-a. Later, we generated the SiO2 rods for the AM anchors. A plasma-enhanced chemical vapor deposition (PECVD) process was conducted to deposit the SiO₂ layer. This step was followed by a lithography step and by a ICP-RIE step defining the final rods' shape (Fig. 5-b). Then, we formed an 150 nm-thick IDT made of aluminum by using sputtering and lift-off processes (Fig. 5-c). This allowed to form the CMRs' top electrodes. Finally, we structurally released the CMRs by using a XeF₂-based isotropic etch (Fig. 5-d). As a final step, we covered the CMRs' pads with a 150 nm-thick Au-layer in order to minimize the pads' contact resistance.

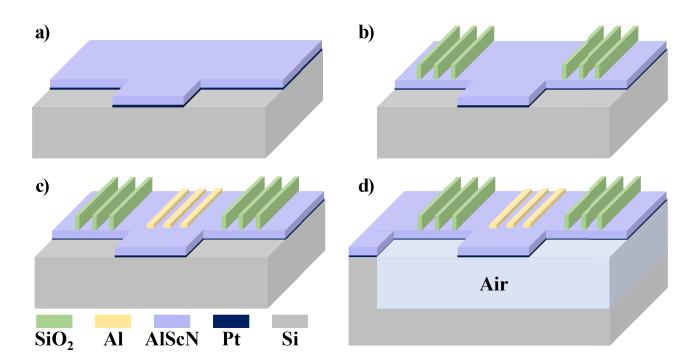


Fig. 5. Main fabrication steps we run for the CMRs with AM anchors demonstrated in this work. (a) After depositing a AlN/Pt/AlScN stack, we formed the release pits used for structurally releasing the devices. (b) Then, we deposited through PECVD and patterned the SiO₂ rods. (c) Next, we deposited and patterned the Al IDTs. (d) Finally, the devices are released.

A Scanned Electron Microscope (SEM) picture of a Device A prototype fabricated in this work is reported in Fig. 1. All the AMs built in this work rely on the same thickness of the SiO₂ layer and the same geometric parameters for the unit-cell listed in the caption of Fig. 1. Also, we used the same finger-width for all the CMRs built in this work.

V. EXPERIMENTAL RESULTS

A. Small Signal

After completing the fabrication, we started our experimental characterization. In order to assess the effectiveness of our AM anchors in confining the acoustic vibration within CMRs' active region, we first analyzed CMRs with AM anchors using different numbers of unit-cells (see Fig. 8-a). For our testing, we probed all the CMRs by using ground-signal-ground probes and by recurring to a vector network analyzer (VNA) for the extraction of the CMRs' admittance curves. As expected, we found a sharp increase with $N_{\rm u}$ of the CMRs' quality factor at the series resonance frequency (Q_s) , with a Q_s reaching a nearly saturated value for N_u =6 (Fig. 6-a). This matches well the expectations based on our FEM analysis (Fig. 2-b). Also, it confirms that six unit-cells are enough to simultaneously minimize the acoustic dissipations while still achieving a low $R_{\rm th}$ value. A trend similar to that of $Q_{\rm s}$ was found for the CMRs' figure-of-merit (FoM) vs. $N_{\rm u}$ (see the yellow curve in Fig. 6-a). We also report (Fig. 6-b) the measured admittance for the highest- Q_s device among all the fabricated replicas of Device A.

To compare the performance, we built replicas of Device B on the same wafer as Device A. We tested 27 and 20 replicas for Device A and Device B respectively. The statistical results for Q_s and FoM are plotted in Fig 7-b,c. We discovered that using AM anchors leads to improved Q_s -values compared to conventional designs with etched lateral sides. We speculate this Q_s -improvement to be related to a mitigation of the mode conversion happening at stress-free boundaries that have sidewall angles lower than 90 degrees (see 7-a). Due to this mode conversion, more energy leaks through the anchors along the y-direction. We also found the k_t^2 for CMRs using AM anchors to slightly reduce compared to conventional designs. This is expected since the device becomes a bit stiffer than the

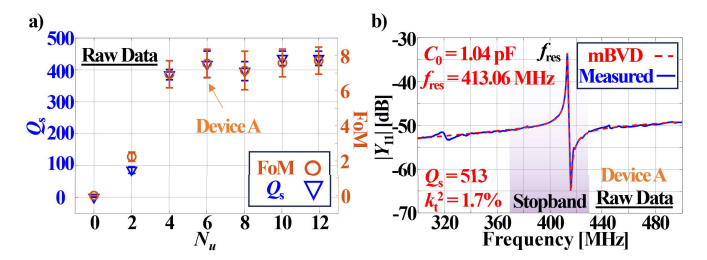


Fig. 6. a) Measured $Q_{\rm S}$ (in blue) and FoM (in orange) vs. $N_{\rm u}$ for the CMRs with AM anchors built in this work. Three devices per configurations were tested. The standard deviation for both $Q_{\rm S}$ and FoM trends are reported; b) Measured admittance (Y_{11}) of the Device A-prototype with the highest- $Q_{\rm S}$ we found in our measurements.

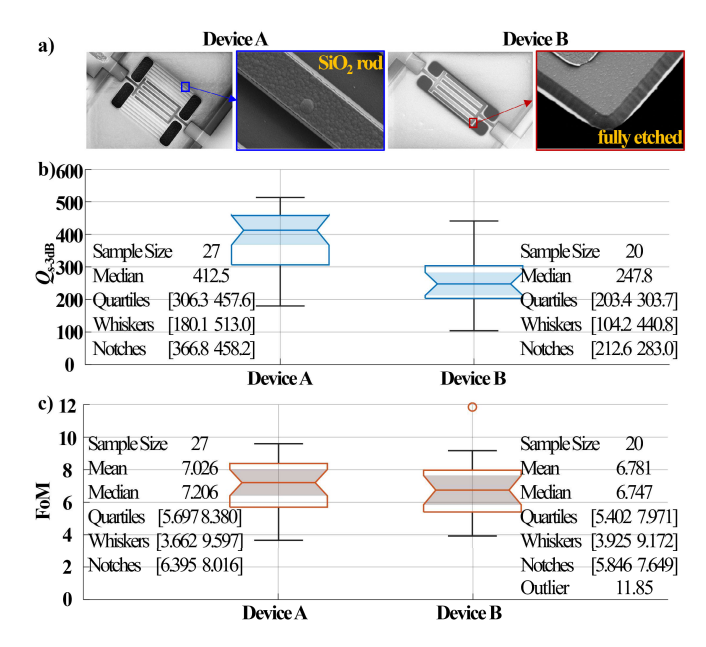


Fig. 7. a) SEM pictures of a CMR with AM anchors (Device A, left) and of one with conventional stress-free boundaries (Device B, right). (b) Averagely measured Q for the CMR designs used by the devices depicted in (a). Evidently, the $Q_{\rm S}$ value of Device A is higher than Device B. (c) Averagely measured FoM for the CMR designs used by the devices depicted in (a). Evidently, the FoM value of Device A is also higher than Device B. The improvement is a bit lower than that detected for the $Q_{\rm S}$ due to a slight reduction of the $k_{\rm f}^2$ for the CMR with AM lateral anchors.

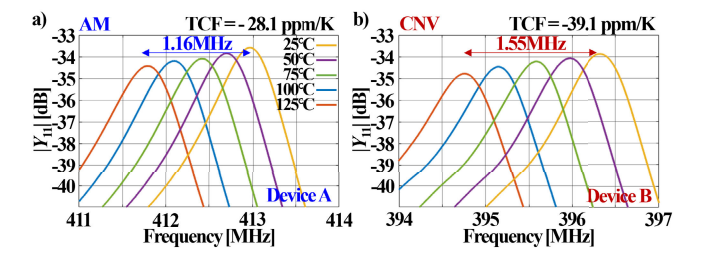


Fig. 8. a) Admittance response around resonance for Device A vs. frequency and vs. temperature. This characterization was run by using a temperature controlled chuck during the device electrical characterization; b) Admittance response around resonance vs. frequency and vs. temperature for Device B. Both characterizations were run by using a temperature controlled chuck during the device electrical testing.

conventional case. Nonetheless, the overall $FoM(=Q_s \cdot k_t^2)$ is higher when using AM anchors rather than fully etched lateral sides.

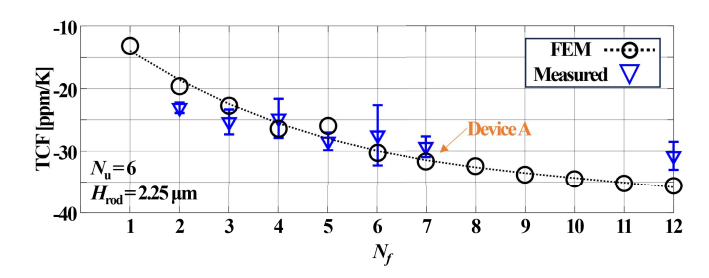


Fig. 9. Measured (blue triangle) and simulated (dashed line, replotted from Fig. 4-b) TCF vs. the number of fingers in the active region for the CMRs reported in this work that use AM anchors and a $N_{\rm u}$ value equal to 6. It is worth mentioning that the TCF of conventional designs with fully-etched lateral sides is 39.1 ppm, as shown in Fig. 8.

B. Temperature Sensitivity

Next, we extracted the TCF for a Device A and compared it to what is attained by a Device B (see Fig. 8). As expected, we found Device A to show a lower TCF (-28.1 ppm/K) compared to Device B (-39.1 ppm/K). This further confirms that using SiO₂ rods to form the AM anchors can not only ensure acoustic energy confinement but also benefits the achievable TCF. To confirm that the achievable TCF is ultimately dependent on the number of fingers in the CMR's active region, we built a set of CMRs with different number of fingers (from 2 to 12) in the active region and with the same AM anchors' design used by Device A. As expected, we found that CMRs with low numbers of fingers exhibit lower |TCF| values than those with high numbers of fingers (see Fig. 9). In fact, the degree of temperature compensation achievable when relying on the SiO₂ rods in our AM anchors is directly proportional to the ratio of the elastic energy stored in the rods to the one stored in CMRs' active region. This last energy term grows proportionally with $N_{\rm f}$.

C. Power Handling

Following this first round of testing, we proceeded with a characterization of the power handling capabilities of the Device A considered in Fig. 8. During this characterization we drove such device with increasing power levels (from -10 dBm to 2 dBm) and repeated the extraction of its admittance for each power level. For this extraction, we set a low IF bandwidth (50Hz) in our VNA. Setting a low IF bandwidth during this measurement is key to provide the tested CMR with enough time to heat-up according to its electrical admittance, thermal characteristics and driving frequency [24], [30]. We found α_d to be 1.7e20 C^{-2} for Device A, which is 6 times lower than what we were able to demonstrate in our previous work when using AM anchors with a corrugated AlScN film [30]. The same extraction was performed for the Device B considered in Fig. 8. We found that the measured α_d for Device A is 57.5% lower than the α_d value (4.0e20 C^{-2}) of the tested Device B (see Fig. 10-b). This further confirms that CMRs with lateral AM anchors can achieve superior power-handling capabilities compared to conventional CMRs with fully-etched lateral sides. It is also worth mentioning that the extraction of α_d was executed through the same procedure discussed in [24]. The measured α_d values can also be

TABLE I LIST OF ACRONYMS

Acronym	Definition
AlScN	Scandium-doped Aluminum Nitride
AM	Acoustic Metamaterials
$\alpha_d^{(an)}$	Duffing nonlinear coefficient (analytical)
C_{th}	Equivalent thermal capacitance
CMR(s)	Contour mode resonator(s)
FEM	Finite element model
$f_{\rm res}$	Frequency of resonance
$f_{ m off}$	Frequency offsets
k_t^2	Effective electromechanical coupling coefficient
ICP	Inductively coupled plasma
LO	Loop oscillator
mBVD	Modified Butterworth-Van Dyke model
mBR	Metal Bragg reflectors
$N_{ m f}$	Number of IDT fingers for CMR
$N_{ m u}$	Number of unit-cells for AM
PECVD	Plasma-enhanced chemical vapor deposition
$Q_{\rm s}$	Series quality factor
RIE	Reactive-ion etching
$R_{ m m}$	Motional resistance of a resonator
R_{s}	Series resistance of a resoantor
$R_{ m th}$	Equivalent thermal resistance
SiO_2	Silicon dioxide
TCE	Thermoelastic coefficient
TCF	Temperature coefficient of frequency
τ_{act}	Thermal time constant
XeF ₂	Xenon difluoride

TABLE II
SUMMARY OF THERMAL NONLINEARITY AND RELATED FACTORS

Property	$R_{\rm th}$	TCF	$R_{\rm m}+R_{\rm s}$	$f_{\rm res}$	α_d^{an}	$\alpha_{ m d}$
Unit	[K/W]	[ppm/K]	$[\Omega]$	[MHz]	$[C^{-2}]$	$[C^{-2}]$
CNV	4.86e4	-39.1	50.7	397.01	5.99e20	4.00e20
AM	2.63e4	-28.1	48.6	413.06	2.42e20	1.70e20

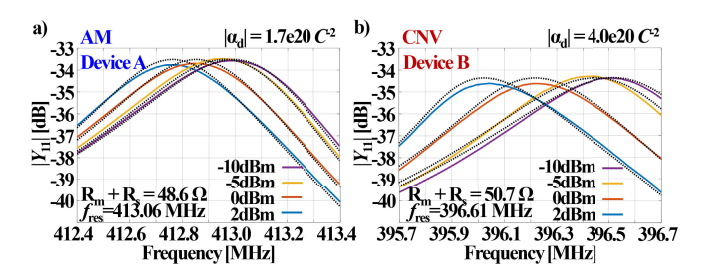


Fig. 10. Admittance responses for increasing power levels and around resonance of Device A (a) and of Device B (b). It is worth mentioning that for both cases, (R_m+R_s) is nearly equal to 50 Ω . So, the power applied during the sweep matches closely the power absorbed at resonance.

compared to the corresponding analytical predictions (labeled as α_d^{an} values for clarity). To extract the α_d^{an} values for Device A and Device B, we relied on a temperature-dependent mBVD model [24] to extract ($R_s + R_m$) and TCF. Also, we used the FEM simulated R_{th} values. All these parameters allow to compute α_d^{an} for both Device A and Device B by using Eq. 1. We found that the α_d values we experimentally extracted for both devices under consideration in Fig. 10 match closely the corresponding α_d^{an} values (2.42e20 C^{-2} for Device A and 5.99e20 C^{-2} for Device B). A summary of analytical and experimental α_d values, along with the related thermal properties, are shown in Table-II.

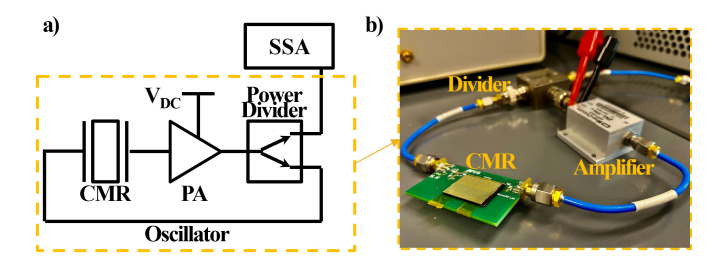


Fig. 11. a) Schematic of the oscillator-circuit topology we have used in this work to characterize the long-term stability of $LO_{\rm CNV}$ and $LO_{\rm AM}$; b) A picture of the assembled circuit including a power splitter (Fairview Microwave MP01500B-2), an amplifier (Mini-Circuits ZKL-1R5+). During our measurements we used a signal-source-analyzer (SSA, Keysight E5055A) for phase-noise extraction.

D. Phase Noise Impact in Oscillators

To provide experimental evidence that reducing CMRs' α_d by using AM anchors is beneficial in RF systems that use CMRs for timing applications, we assembled two feedback-loop oscillators (LOs). One oscillator (labeled as LO_{CNV}) uses the Device B prototype discussed in Fig. 10-b as the frequency-setting resonant component. The other one (labeled as LO_{AM}) uses the Device A prototype discussed in Fig. 10-a. Both oscillators rely on the same topology (Fig. 11) and on identical electronic off-the-shelf components listed in Fig. 11. Also, both oscillators were characterized by connecting their output (i.e., one of the ports of a twoways power-splitter) to a signal source analyzer (SSA) A schematic of the circuit we used to characterize the stability of LO_{CNV} and LO_{AM} is reported in Fig. 11, together with a picture of the actual set-up we assembled for LO_{AM} in our laboratory. During the performance characterization of both oscillators, we specifically looked at their short-term stability for high power levels in their CMR. Being able to achieve large short-term stability (i.e., low close-in phase-noise or, equivalently, low RMS jitter values for frequency offsets, f_{off} , between 10KHz to 1 MHz) for increasing power levels in the CMR is particularly of interest for sensing applications. In fact, when CMRs are used as sensors in closed-loop sensing schemes, their limit-of-detection can be reduced by increasing the dynamic range of the oscillator circuit used for reading-out their resonance frequency. Yet, such increase of dynamic range is only achievable when CMRs can tolerate higher-power driving signals, which is generally challenging due to their strong thermal nonlinearities. While few previous studies have shown that relying on Duffing nonlinearities in CMR-based LOs gives access to special operating points affected by lower phase-noise levels in the close-in region ([24]), it is practically very hard to continuously and stably operate at such working points. As a result, for almost all cases, CMRs' Duffing nonlinearities produce a degradation of the phase-noise response caused by a stronger amplitude-tophase-noise conversion for increasing power levels driving the resonator. Consequently, the thermal nonlinearities affecting CMRs is ultimately the main limiting factor for the limit-ofdetection of any closed-loop sensing system based on their use.

TABLE III
RESULTS OF THE PHASE NOISE CHARACTERIZATIONS

P [dBm]	$V_{\rm dc}$ [V]		$\Delta f \text{ [MHz]}$		RMS Jitter [sec]	
AM/CNV	AM	CNV	AM	CNV	AM	CNV
1.2	6.0	6.1	0	0	7.32e-13	6.63e-13
1.6	6.1	6.2	-0.12	-0.14	7.25e-13	7.42e-13
2.5	6.4	6.4	-0.42	-0.45	7.07e-13	7.41e-13
3.7	7.0	6.8	-0.58	-1.27	5.43e-13	5.11e-13
4.0	7.2	7.0	-0.65	-1.79	5.78e-13	5.55e-13
4.9	7.8	7.5	-0.82	-2.99	5.58e-13	1.89e-12
5.1	8.0	7.6	-0.83	-3.12	7.89e-13	9.23e-13
5.4	8.2	7.8	-1.19	-3.35	6.06e-13	8.39e-13

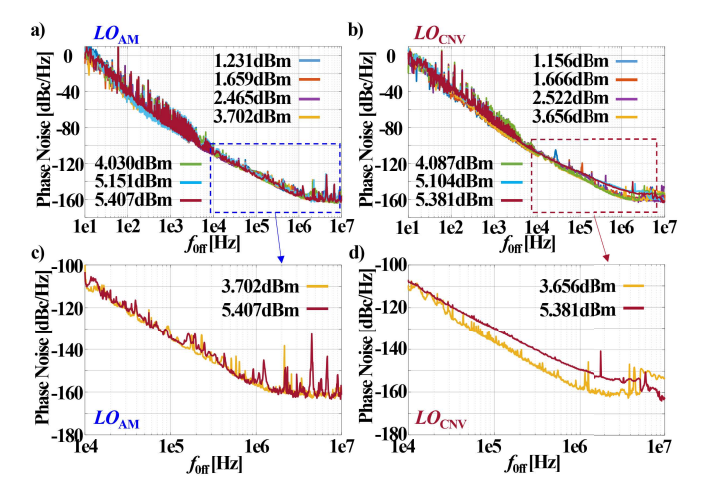


Fig. 12. Measured phase-noise levels of $LO_{\rm AM}$ (a,c) and $LO_{\rm CNV}$ (b,d) for increasing output power levels [i.e., for increasing dc-volgates (from 6V to 8.2V) biasing the amplifier used in the oscillator].

As mentioned earlier, the use of AM anchors allows to reduce α_d compared to conventional CMRs with fully-etched lateral sides. Due to the relatively low $(R_{\rm m}+R_{\rm s})$ value ($\sim 50\Omega$) for both CMRs under consideration, the bias-voltage $(V_{\rm dc})$ of the amplifier used to sustain the oscillation in both loops can be largely increased. The increase of $V_{\rm dc}$ beyond the minimum bias voltage (V_{dc} =6V) allows to boost the minimum loop-gain required to start the oscillation. As a result, tuning $V_{\rm dc}$ allows to control the oscillator's output power, as well as the power driving the resonator. We can compare the phase-noise profile of LO_{AM} with LO_{CNV} for different V_{dc} values. This allows to assess to the phase-noise performance of both oscillators for different power levels driving their CMRs. As evident from Fig. 12, LO_{AM} and LO_{CNV} exhibit closely matching phase-noise profiles up to the floor-region for output power levels up to ~ 3 dBm. However, for output power levels beyond \sim 3 dBm, LO_{CNV} exhibits progressively more degraded phase-noise values for f_{off} values higher than 10 kHz, differently from the phase-noise profile of LO_{AM} that remains almost unaltered. As a further confirmation of the higher short-term frequency stability of LO_{AM} compared to LO_{CNV}, we also report in Table III RMS jitter levels (for frequency offsets up to 1 MHz) vs. $V_{\rm dc}$ (and the corresponding output power levels) for both LO_{AM} and LO_{CNV} . As expected, we found that LO_{AM} exhibits lower RMS jitter levels for V_{dc} higher than 7V, corresponding to output power levels higher than ~ 3 dBm. We also extracted the output frequency shift

 (Δf) for both $LO_{\rm CNV}$ and $LO_{\rm AM}$ induced by self-heating when sweeping $V_{\rm dc}$. As expected, we found that $LO_{\rm AM}$ undergoes a smaller frequency shift than $LO_{\rm CNV}$ due to the lower TCF of its CMR. A summary of all our findings is provided in Table III.

VI. CONCLUSION

In this work, we have demonstrated a new type of AM anchors for CMRs. These new anchors do not rely on a corrugated AlScN film to form their AM structure. Instead, they rely on SiO₂ rods deposited on the same AlScN film used for the CMRs' active region. The new AM anchors' design reported in this work allows to further reduce the CMR's R_{th} with respect to conventional CMR-designs using fully-etched lateral sides. Moreover, using SiO₂ rods to form the reported AM structures allows to achieve a degree of temperature compensation. As a result, the CMRs' nonlinear Duffing term further decreases compared to what has been achieved in previous AM anchors' demonstrations. We have also demonstrated that using a CMR with the reported AM anchors as the frequency setting component in an oscillator allows to enhance the short-term stability compared to what achievable with a conventional CMR with fully-etched lateral sides.

REFERENCES

- [1] R. C. Ruby, P. Bradley, Y. Oshmyansky, A. Chien, and J. D. Larson, "Thin film bulk wave acoustic resonators (FBAR) for wireless applications," in *Proc. IEEE Ultrason. Symp.*, Oct. 2001, pp. 813–821.
- [2] G. Piazza, P. J. Stephanou, and A. P. Pisano, "Piezoelectric aluminum nitride vibrating contour-mode MEMS resonators," *J. Microelec-tromech. Syst.*, vol. 15, no. 6, pp. 1406–1418, Dec. 2006. [Online]. Available: http://ieeexplore.ieee.org/document/4020287/
- [3] V. Yantchev and I. Katardjiev, "Thin film Lamb wave resonators in frequency control and sensing applications: A review," J. Micromech. Microeng., vol. 23, no. 4, Apr. 2013, Art. no. 043001, doi: 10.1088/0960-1317/23/4/043001.
- [4] Y. Hou, M. Zhang, G. Han, C. Si, Y. Zhao, and J. Ning, "A review: Aluminum nitride MEMS contour-mode resonator," *J. Semicond.*, vol. 37, no. 10, Oct. 2016, Art. no. 101001. [Online]. Available: https://iopscience.iop.org/article/10.1088/1674-4926/37/10/101001
- [5] C. Cassella and M. Rinaldi, "Cross-sectional Lamé mode contiguous filters for next-generation LTE-advanced platforms," in *IEEE MTT-S Int. Microw. Symp. Dig.*, May 2016, pp. 1–3.
- [6] X. Zhao, L. Colombo, and C. Cassella, "Aluminum nitride two-dimensional-resonant-rods," Appl. Phys. Lett., vol. 116, no. 14, Apr. 2020, Art. no. 143504, doi: 10.1063/5.0005203.
- [7] Y. Liu, Y. Cai, Y. Zhang, A. Tovstopyat, S. Liu, and C. Sun, "Materials, design, and characteristics of bulk acoustic wave resonator: A review," *Micromachines*, vol. 11, no. 7, p. 630, Jun. 2020. [Online]. Available: https://www.mdpi.com/2072-666X/11/7/630
- [8] R. Ruby, P. Bradley, D. Clark, D. Feld, T. Jamneala, and K. Wang, "Acoustic FBAR for filters, duplexers and front end modules," in *IEEE MTT-S Int. Microw. Symp. Dig.*, Jun. 2004, pp. 931–934. [Online]. Available: https://ieeexplore.ieee.org/document/1339128
- [9] M. Rinaldi, C. Zuniga, C. Zuo, and G. Piazza, "Super-high-frequency two-port AlN contour-mode resonators for RF applications," *IEEE Trans. Ultrason., Ferroelectr., Freq. Control*, vol. 57, no. 1, pp. 38–45, Jan. 2010.
- [10] A. Gao, K. Liu, J. Liang, and T. Wu, "AIN MEMS filters with extremely high bandwidth widening capability," *Microsystems Nano-engineering*, vol. 6, no. 1, pp. 1–11, Sep. 2020. [Online]. Available: https://www.nature.com/articles/s41378-020-00183-5
- [11] M. Schneider, M. DeMiguel-Ramos, A. J. Flewitt, E. Iborra, and U. Schmid, "Scandium aluminium nitride-based film bulk acoustic resonators," in *Proc. MDPI*, 2017, vol. 1, no. 4, p. 305. [Online]. Available: https://www.mdpi.com/2504-3900/1/4/305

- [12] L. Colombo, A. Kochhar, C. Xu, G. Piazza, S. Mishin, and Y. Oshmyansky, "Investigation of 20% scandium-doped aluminum nitride films for MEMS laterally vibrating resonators," in *Proc. IEEE Int. Ultrason. Symp. (IUS)*, Sep. 2017, pp. 1–4.
- [13] X. Zhao and C. Cassella, "On the coupling coefficient of ScyAl1-yN-based piezoelectric acoustic resonators," in *Proc. Joint Conf. IEEE Int. Freq. Control Symp. Eur. Freq. Time Forum (EFTF/IFC)*, Apr. 2019, pp. 1–4.
- [14] A. Lozzi, E. Ting-Ta Yen, P. Muralt, and L. G. Villanueva, "Al_{0.83}Sc_{0.17}N contour-mode resonators with electromechanical coupling in excess of 4.5%," *IEEE Trans. Ultrason., Ferroelectr., Freq. Control*, vol. 66, no. 1, pp. 146–153, Jan. 2019.
- [15] M. Park and A. Ansari, "Epitaxial Al_{0.77}Sc_{0.23}N SAW and Lamb wave resonators," in *Proc. Joint Conf. IEEE Int. Freq. Control Symp. Int.* Symp. Appl. Ferroelectr. (IFCS-ISAF), Jul. 2020, pp. 1–3.
- [16] G. Esteves et al., "Al_{0.68}Sc_{0.32}N Lamb wave resonators with electromechanical coupling coefficients near 10.28%," *Appl. Phys. Lett.*, vol. 118, no. 17, Apr. 2021, Art. no. 171902, doi: 10.1063/5.0047647.
- [17] X. Zhao et al., "A 5.3 GHz Al_{0.76}Sc_{0.24}N two-dimensional resonant rods resonator with a k_t² of 23.9%," *J. Microelectromech. Syst.*, vol. 31, no. 4, pp. 561–570, Aug. 2022.
- [18] M. Assylbekova, M. Pirro, X. Zhao, G. Michetti, P. Simeoni, and M. Rinaldi, "Study of the performance enhancement of sc-doped AlN super high frequency cross-sectional Lamé mode resonators," *Micromachines*, vol. 14, no. 3, p. 515, Feb. 2023. [Online]. Available: https://www.mdpi.com/2072-666X/14/3/515
- [19] G. A. Slack, R. A. Tanzilli, R. O. Pohl, and J. W. Vandersande, "The intrinsic thermal conductivity of AIN," J. Phys. Chem. Solids, vol. 48, no. 7, pp. 641–647, Jan. 1987. [Online]. Available: https://www.sciencedirect.com/science/article/pii/0022369787901533
- [20] V. Moraes et al., "Thermal conductivity and mechanical properties of AlN-based thin films," J. Appl. Phys., vol. 119, no. 22, Jun. 2016, Art. no. 225304, doi: 10.1063/1.4953358.
- [21] Y. Song et al., "Thermal conductivity of aluminum scandium nitride for 5G mobile applications and beyond," ACS Appl. Mater. Interfaces, vol. 13, no. 16, pp. 19031–19041, Apr. 2021, doi: 10.1021/acsami.1c02912.
- [22] J. D. Larson, J. D. Ruby, R. C. Bradley, J. Wen, S.-L. Kok, and A. Chien, "Power handling and temperature coefficient studies in FBAR duplexers for the 1900 MHz PCS band," in *Proc. IEEE Ultrason. Symp.*, Oct. 2000, pp. 869–874.
- [23] O. Wunnicke, P. J. van der Wel, R. C. Strijbos, and F. de Bruijn, "Thermal behavior of BAW filters at high RF power levels," *IEEE Trans. Ultrason., Ferroelectr., Freq. Control*, vol. 56, no. 12, pp. 2686–2692, Dec. 2009. [Online]. Available: https://ieeexplore.ieee. org/document/5307500
- [24] J. Segovia-Fernandez and G. Piazza, "Thermal nonlinearities in contour mode AlN resonators," *J. Microelectromech. Syst.*, vol. 22, no. 4, pp. 976–985, Aug. 2013.
- [25] J. Segovia-Fernandez and G. Piazza, "Thermoelastic damping in the electrodes determines Q of AlN contour mode resonators," J. Microelectromech. Syst., vol. 26, no. 3, pp. 550–558, Jun. 2017.
- [26] Y. Zheng, M. Park, A. Ansari, C. Yuan, and S. Graham, "Self-heating and quality factor: Thermal challenges in aluminum scandium nitride bulk acoustic wave resonators," in *Proc. 21st Int. Conf. Solid-State Sensors, Actuat. Microsystems (Transducers)*, Jun. 2021, pp. 321–324. [Online]. Available: https://ieeexplore.ieee. org/document/9495613/authors#authors
- [27] J. Segovia-Fernandez, M. Cremonesi, C. Cassella, A. Frangi, and G. Piazza, "Anchor losses in AlN contour mode resonators," *J. Micro-electromech. Syst.*, vol. 24, no. 2, pp. 265–275, Apr. 2015.
- [28] J. Segovia-Fernandez, M. Cremonesi, C. Cassella, A. Frangi, and G. Piazza, "Experimental study on the impact of anchor losses on the quality factor of contour mode AlN resonators," in *Proc. 17th Int. Conf. Solid-State Sensors, Actuat. Microsystems*, Jun. 2013, pp. 2473–2476.
- [29] X. Zhao, O. Kaya, M. Pirro, S. Kang, and C. Cassella, "Improving thermal linearity and quality factor of Al₇₂Sc₂₈N contour mode resonators using acoustic metamaterials based lateral anchors," in *Proc. Joint Conf. Eur. Freq. Time Forum IEEE Int. Freq. Control Symp. (EFTF/IFCS)*, Apr. 2022, pp. 1–3.
- [30] X. Zhao, O. Kaya, M. Pirro, P. Simeoni, J. Segovia-Fernandez, and C. Cassella, "Extending the linearity of AlScN contour-mode-resonators through acoustic metamaterials-based reflectors," *IEEE Trans. Ultrason.*, Ferroelectr., Freq. Control, vol. 70, no. 10, pp. 1229–1238, Oct. 2023. [Online]. Available: https://ieeexplore.ieee.org/abstract/document/10045740

- [31] C. Zuo, J. Van Der Spiegel, and G. Piazza, "1.05-GHz CMOS oscillator based on lateral- field-excited piezoelectric AlN contour-mode MEMS resonators," *IEEE Trans. Ultrason., Ferroelectr., Freq. Control*, vol. 57, no. 1, pp. 82–87, Jan. 2010.
- [32] Z. Qian, Y. Hui, F. Liu, S. Kang, S. Kar, and M. Rinaldi, "Graphene-aluminum nitride NEMS resonant infrared detector," *Microsyst. Nanoeng.*, vol. 2, no. 1, pp. 1–7, Jun. 2016. [Online]. Available: https://www.nature.com/articles/micronano201626
- [33] E. T.-T. Yen et al., "Programmable oscillator implementation using 2.5 GHz mirror-encapsulated BAW resonator to achieve ±20 PPM overall stability," in *Proc. IEEE Int. Ultrason. Symp. (IUS)*, Oct. 2022, pp. 1–4. [Online]. Available: https://ieeexplore.ieee.org/document/9958706
- [34] M. Agarwal et al. (2006). Amplitude Noise Induced Phase Noise in Electrostatic MEMS Resonators. Accessed: Mar. 4, 2024. [Online]. Available: https://api.semanticscholar.org/CorpusID:4980622
- [35] K. L. Ekinci, Y. T. Yang, and M. L. Roukes, "Ultimate limits to inertial mass sensing based upon nanoelectromechanical systems," *J. Appl. Phys.*, vol. 95, no. 5, pp. 2682–2689, Mar. 2004, doi: 10.1063/1.1642738.
- [36] G. Duffing, Erzwungene Schwingungen Bei Veränderlicher Eigenfrequenz Und IHRE Technische Bedeutung (Sammlung Vieweg HFT). F. Vieweg & Sohn, sec. 6, 1918, p. 134.
- [37] I. Kovacic and M. J. Brennan, The Duffing Equation: Nonlinear Oscillators and Their Behaviour. Chichester, U.K.: Wiley, 2011.
- [38] N. Miller and G. Piazza, "Nonlinear dynamics in aluminum nitride contour-mode resonators," *Appl. Phys. Lett.*, vol. 104, no. 1, Jan. 2014, Art. no. 014102, doi: 10.1063/1.4861461.
- [39] T.-T. Wu, Z.-G. Huang, T.-C. Tsai, and T.-C. Wu, "Evidence of complete band gap and resonances in a plate with periodic stubbed surface," *Appl. Phys. Lett.*, vol. 93, no. 11, Sep. 2008, Art. no. 111902, doi: 10.1063/1.2970992.
- [40] K. Hirao, K. Tanaka, S. Furukawa, and N. Soga, "Anomalous temperature dependence of the sound velocities of SiO₂-TiO₂ glasses," *J. Mater. Sci. Lett.*, vol. 14, no. 10, pp. 697–699, 1995, doi: 10.1007/bf00253375.
- [41] E. Rocas, C. Collado, J. C. Booth, E. Iborra, and R. Aigner, "Unified model for bulk acoustic wave resonators' nonlinear effects," in *Proc. IEEE Int. Ultrason. Symp.*, Sep. 2009, pp. 880–884. [Online]. Available: https://ieeexplore.ieee.org/document/5441686
- [42] D. A. Feld, D. S. Shim, S. Fouladi, and F. Bayatpur, "Advances in nonlinear measurement & modeling of bulk acoustic wave resonators (invited)," in *Proc. IEEE Int. Ultrason. Symp.*, Sep. 2014, pp. 264–272. [Online]. Available: https://ieeexplore.ieee.org/document/6931724



Xuanyi Zhao received the B.S. degree in applied physics from Xi'an Jiaotong University (XJTU), Xi'an, China, in 2015, and the M.S. and Ph.D. degrees in electrical engineering from Northeastern University, Boston, MA, USA, in 2022 and 2024, respectively. His Ph.D. research has focused on micro acoustic metamaterials (μ AMs) for innovative RF MEMS, such as AlN/AlScN micro acoustic μ AMs-based resonators with applications of RF filters, oscillators, and sensors. In 2023, he was an Intern Research Engineer at Texas Instruments Inc.,

Kilby Labs. His recent work was accepted for publication as Hilton Head 2024 Solid-State Sensors, Actuators and Microsystems Workshop for Late News. In 2022, he won the Best Paper Award from the IEEE International Frequency Control Symposium (IFCS). One of his previous journal articles was selected as a featured article by the *Applied Physics Letters* magazine.



Onurcan Kaya received the B.S. and M.S. degrees in mechanical engineering from Middle East Technical University (METU), Ankara, Turkey, in 2014 and 2017, respectively. He is currently pursuing the Ph.D. degree with the Department of Electrical and Computer Engineering, Northeastern University, Boston, MA, USA. His research interests include the design, fabrication, and characterization of MEMS devices, particularly capacitive resonant sensors, piezoelectric microacoustic resonators, piezoelectric microacoustic filters, and ferroelectric varactors.



Tommaso Maggioli received the B.S. degree in engineering physics and the M.S. degree in nanotechnologies for ICTs from Politecnico di Torino, Turin, Italy, in 2020 and 2023, respectively. He is currently pursuing the Ph.D. degree with the Department of Electrical and Computer Engineering, Northeastern University, Boston, MA, USA. His current research interests include micro-acoustic radio frequency (RF) devices based on piezoelectric materials and acoustic metamaterials.



Cristian Cassella (Member, IEEE) received the B.S.E. and M.Sc. degrees (Hons.) from the University of Rome Tor Vergata, in 2006 and 2009, respectively, and the Ph.D. degree from Carnegie Mellon University, in 2015. In 2011, he was a Visiting Scholar with the University of Pennsylvania. In 2015, he was a Post-Doctoral Research Associate at Northeastern University, Boston, MA, USA. In 2018, he became an Assistant Professor. He is currently an Associate Professor with the Department of Electrical and Computer Engineering,

Northeastern University. He is the author of more than 100 publications in peer-reviewed journals and conference proceedings. Two of his peer-reviewed journal articles published in IEEE JOURNAL OF MICROELECTROMECHAN-ICAL SYSTEMS (JMEMS) were selected as Papers of Excellent Quality (JMEMS RightNowPapers), hence being released as open-access. One of his journal articles was chosen as the cover for the Nature Nanotechnology October 2017 Issue. Another one of his journal articles was selected as a featured article by the Applied Physics Letters magazine. He holds seven patents and four patent applications in the area of acoustic resonators and RF systems. In 2018, he was awarded by the European Community (EU) the Marie-Sklodowska-Curie Individual Fellowship. In 2021, he was a recipient of the NSF CAREER Award. He received the Best Student Paper Award from the IEEE International Frequency Control Symposium in 2013, 2021, 2022, and 2023 (with his students). He is a Technical Reviewer of several journals, such as Applied Physics Letters, IEEE TRANSACTIONS ON ELECTRON DEVICES, IEEE TRANSACTIONS ON ULTRASONICS, FERROELECTRIC AND FREQUENCY CONTROL, IEEE JOURNAL OF MICROELECTROMECHANICAL SYSTEMS, IEEE ELECTRON DEVICE LETTERS, Journal of Micromechanics and Microengineering, Journal of Applied Physics, IEEE SENSORS LETTERS, and Review of Scientific Instruments.